

PAPER

Multi-step material decomposition for spectral computed tomography

To cite this article: Nathaniel R Fredette et al 2019 Phys. Med. Biol. 64 145001

View the <u>article online</u> for updates and enhancements.

Physics in Medicine & Biology





RECEIVED

7 September 2018

REVISED 10 May 2019

ACCEPTED FOR PUBLICATION 19 June 2019

PUBLISHED 11 July 2019 PAPER

Multi-step material decomposition for spectral computed tomography

Nathaniel R Fredette¹, Amar Kavuri¹ and Mini Das^{1,2,3}

- Department of Biomedical Engineering, University of Houston, Houston, TX 77204, United States of America
- ² Department of Physics, University of Houston, Houston, TX 77204, United States of America
- 3 Author to whom correspondence should be addressed.

E-mail: mdas@uh.edu

Keywords: photon counting spectral detectors, material decomposition, spectral CT, spectral x-ray, algorithm

Abstract

Spectral images from photon counting detectors are being explored for material decomposition applications such as for obtaining quantitative maps of tissue types and contrast agents. While these detectors allow acquisition of multi-energy data in a single exposure, separating the total photon counts into multiple energy bins can lead to issues of count starvation and increased quantum noise in resultant maps. Furthermore, the complex decomposition problem is often solved in a single inversion step making it difficult to separate materials with close properties. We propose a multi-step decomposition method which allows solving the problem in multiple steps using the same spectral data collected in a single exposure. During each step, quantitative accuracy of a single material is under focus and one can flexibly optimize the bins chosen in that step. The result thus obtained becomes part of the input data for the next step in the multi-step process. This makes the problem less ill-conditioned and allows better quantitation of more challenging materials within the object. In comparison to a conventional single-step method, we show excellent quantitative accuracy for decomposing up to six materials involving a mix of soft tissue types and contrast agents in micro-CT sized digital phantoms.

1. Introduction

Existing dual energy techniques such as temporally sequential scanning, rapid kVp switching, multilayer detectors or dual x-ray sources allow one to obtain two spectrally separated measurements, which can be used in material discrimination of medical and biological samples. Although these methods are often compatible with existing clinical technologies, they often suffer from incomplete spectral separation, require temporal image registration or require additional hardware or software (McCollough *et al* 2015). With the emergence of photon counting detectors (PCDs) (Taguchi and Iwanczyk 2013), acquiring multi-energy x-ray data via a single low dose acquisition is possible. PCDs, still in the research and development stages, pose their own challenges such as detector distortions and the fabrication of large area detectors with high atomic number sensors. While techniques are being developed to mitigate and correct spectral distortions as well as fabricate these large sensors (Ballabriga *et al* 2013, Jakubek *et al* 2014), availability of several energy bins at once offers the possibility to discriminate between more materials than conventional dual energy techniques. Although still in early stages of clinical adaptation, material discrimination has the potential for wide applicability in both clinical and industrial settings and could accompany routine CT scans. A couple of the proposed clinical applications are breast and brain cancer imaging (Alvarez and Macovski 1976, Le *et al* 2011, Le and Molloi 2011, Lee *et al* 2014) among many others.

A method for obtaining maps of constituent materials from spectral data was first proposed for projection domain by Alvarez and Macovski (1976) and implemented in tomographic image domain by Brooks (1977). In the projection domain approach, one attempts to resolve the object into basis material thickness maps knowing these constituent material concentrations or densities (Alvarez and Macovski 1976, Yu *et al* 2009, Schmidt and Petkas 2011, Lee *et al* 2014). These approaches have been executed using both dual energy strategies (Alvarez and Macovski 1976, Yu *et al* 2009) and PCDs (Schmidt and Petkas 2011, Lee *et al* 2014). In image domain methods,

the three-dimensional (3D) spectral attenuation maps of the composite materials are first obtained. This information is then used for decomposition (Liu *et al* 2009, Le *et al* 2011, Le and Molloi 2011, Alessio and MacDonald 2013, Lee *et al* 2014, Mendonca *et al* 2014, Niu *et al* 2014, Li *et al* 2015, Xue *et al* 2017). A third approach, such as the ones explained in Cai *et al* (2013), Long and Fessler (2014), Barber *et al* (2016), Chung *et al* (2010), can be used to directly estimate basis material images from binned raw projection data.

While PCDs offer the advantage of yielding multiple energy bin data at once, thereby reducing radiation dose and imaging time, photon starvation per energy bin can be an issue. This results in increased noise levels in the data and decomposition maps for the same photon flux and imaging time. Solving for a larger number of unknowns using fewer energy bin data to increase photon economy can make the problem ill-conditioned when decomposing a multi-material object. To mitigate these issues, we recently proposed a multi-step decomposition technique which solves for the decomposed map of each material step-by-step (Fredette *et al* 2017). In each step the optimal combination of energy bins can be chosen or in special cases some bins can be combined to improved photon economy. Retrieval results from each step act as added information to the data in subsequent steps, thereby allowing iterative improvement in the results. Material specific energy weighting in each step of the multi-step algorithm has also been displayed promoting further utility of this method (Fredette *et al* 2018).

In many material decomposition methods, the composite object is separated into spatial material concentration distributions in terms of grams per cubic centimeter or molar concentrations (Liu et al 2009, Yu et al 2009, Le et al 2011, Le and Molloi 2011, Ronaldson et al 2012, Alessio and MacDonald 2013, Li et al 2015). In our method, however, the object is decomposed into spatial volume fraction distributions (Ronaldson et al 2012, Lee et al 2014, Long and Fessler 2014, Mendonca et al 2014, Xue et al 2017). These techniques are mostly equivalent except for some minor differences. In the volume fraction map technique, an assumption about the mass densities of the materials in the object is required, where as in the concentration map techniques it is not. Both techniques allow for the incorporation of a simple conservation of volume, sum-to-one constraint. The volume fraction map techniques also permit the use of convenient bounds of zero and one during the bounded least squares solution as this range captures all physically meaningful solutions. This constraint equation and bounding during the solution process helps to control the results and prohibit non-physical solutions that are possible with simple linear least squares. The bounds would be problem specific for the concentration based techniques and most likely vary for each material.

Most current material characterization techniques can accurately separate two (Alvarez and Macovski 1976, Maass et al 2009, Niu et al 2014, Zbijewski et al 2014), three (Granton et al 2008, Liu et al 2009, Yu et al 2009, Ronaldson et al 2012, Kappler et al 2013, Koenig et al 2014, Lee et al 2014, Li et al 2015) or four (Le et al 2011, Le and Molloi 2011, Alessio and MacDonald 2013, Kappler et al 2013) materials. The ability to distinguish between more than four materials has been investigated for various applications with dual energy imaging (Long and Fessler 2014, Mendonca et al 2014, Xue et al 2017, Ding et al 2018). In phantom studies, the ability to distinguish between the six materials of Teflon, Delrin, iodine, polymethylpentene, soft-tissue and air has been demonstrated (Xue et al 2017, Ding et al 2018). The common method for increasing the number of materials that can be decomposed is through the incorporation of constraints such as conservation of volume and mass. Another common way is to limit the number of basis materials in each voxel via additional constraints. In one approach using PCDs, the decomposition is broken into a segmentation step and a quantification step where the former limits the number of possible materials in each voxel to one (Le et al 2011, Le and Molloi 2011). In other dual energy approaches, the number of basis materials in each voxel is limited to three because of the three equations of the two energy-resolved measurements of the dual energy technique and the conservation of volume constraint (Long and Fessler 2014, Mendonca et al 2014, Xue et al 2017). Except for Mendonca et al (2014), all of these methods formulate the decomposition as an optimization problem where iteration is used to minimize a merit function. This iteration can lead to longer solution times making parallelization crucial to the implementation of these algorithms.

Our proposed multistep decomposition method is detailed in sections below. Here we do not limit the number of materials allowed per voxel allowing more complex material compositions, further we have fewer constraints than several other proposed methods. We demonstrate the method via simulated phantom experiments. We begin by describing the simulation platform and the detector model in section 2.1. The existing single-step and newly proposed multi-step methods are then described in sections 2.2 and 2.3, respectively. In sections 2.8–2.10, three examples of a four-material problem, a six-material problem and a four-material, mixed-material problem will be discussed to illustrate the method. Section 3 will reiterate some of the strengths and limitations of the multi-step decomposition technique and provide concluding remarks.

2. Materials and methods

2.1. Simulation platform and PCD model

The simulation platform derives from a serial cascade model (Siewerdsen and Jaffray 2000) where the source, object and detector were all treated analytically (Das *et al* 2011, Vedula *et al* 2003). The source was modeled using

the tungsten anode spectral model using interpolating polynomials (TASMIP) method with a tube peak voltage of 120 kVp. An aluminum filter was applied to the source spectrum to reduce lower energy photons which only minimally contribute to image formation and significantly increase patient dose. A total CT dose of 7.92 mGy was applied to 360 projections over a full arc of 360°. The object was modeled as cylinders of various tissue-like or contrast agent materials. The detector was modeled with a cadmium telluride (CdTe) sensor with square pixels of dimension 110 μ m, a thickness of one millimeter and capable of simultaneously recording photon counts for up to eight energy bins similar to the Medipix 3RX developed at CERN (Geneva, Switzerland). Here we use the maximum number of energy bins provided by the Medipix detector to maximize the information recorded. Otherwise, the detector was modeled to have an ideal response with the corresponding CdTe efficiency.

Before performing material decomposition, energy-resolved, raw flat field and object projection data must be simulated or measured with eight energy bins. This was done by simulating the x-ray projections at every keV until the tube peak voltage. Equal count bins were then defined by dividing the simulated x-ray energy spectrum into eight bins and the data at each keV was then summed to form the data corresponding to each bin. Poisson noise was then added to the binned flat field and object data so that the data would have suitable statistics. The focal spot size of the source was modeled via a Gaussian blur. If unequal count bins were obtained, a simple weighting scheme based on contrast to noise ratio (CNR) could be employed to overcome the unequal noise statistics [Schmidt 2009, 2010, Kalluri et al 2013]. The degraded projection data was then filtered via a Wiener filter with a kernel size of 3×3 to reduce the impacts of this Poisson noise. This smallest possible kernel size was found to provide adequate noise reduction with minimal blurring of material edges (Fredette et al 2018). These flat field corrected projection data for each energy bin were reconstructed into 3D volumes representing object attenuation. In this case we employ simple filtered back projection with a voxel size that is slightly larger than the pixel size of 119 μ m \times 119 μ m \times 119 μ m to improve signal to noise ratio (SNR). The data is filtered again to remove residual noise left over after counts filtration and image reconstruction using a Wiener filter of kernel size 5×5 . It has been shown that a Wiener filter can be used to reduce noise in both projections and reconstructions while maintaining small signals such as microcalcifications (Vieira et al 2013). Because of the small 2 cm diameter of the phantoms explored in this work, beam hardening was found to be minimal. However, if larger phantoms are of interest, the reconstructed attenuation from each energy bin could be corrected for beam hardening using a method similar to Le et al (2011). Finally, the decomposition was solved using bounded variable least squares with bounds of zero and one on all of the unknowns in accordance with the method explained in Coleman and Li (1996). This algorithm is the basis for the built-in MATLAB solver *Isqlin* making it easy to implement, parallelizable and computationally efficient. The bounds of zero and one can be relaxed slightly to improve the decomposition results. Box constraints and the sum-to-one constraint are common to many methods (Mendonca et al 2014, Xue et al 2017, Ding et al 2018). Constrained least squares is also commonly used in decomposition problems (Li et al 2015, Ronaldson et al 2012).

2.2. Single-step material decomposition method

In a conventional single-step material decomposition similar to Le *et al* (2011), Le and Molloi (2011), Alessio and MacDonald (2013), Koenig *et al* (2014), Lee *et al* (2014), Persson *et al* (2014) and Li *et al* (2015), the spatial distributions of basis materials are found simultaneously using spectral data from a PCD. For N available energy bins indexed by j, one can reconstruct N spectrally varying CT images of the object and one additional CT image representing the conservation of volume constraint. If we represent these multi-energy 3D attenuation maps as $\vec{\mu}(E_j, \vec{r})$ and assume that the material is composed of M basis materials, one can write the decomposition model as

$$\vec{\mu}(E_j, \vec{r}) = \sum_{i}^{M} \mu_i(E_j) \vec{f}_i(\vec{r}), \tag{1}$$

where $\vec{f_i}(\vec{r})$ denotes the respective volume fractions for each basis material i. In equation (1), E_j represents the energy corresponding to the median counts within bin j based on the x-ray energy spectrum and \vec{r} is the spatial variable. In a single-step decomposition technique, one attempts to solve for the volume fraction maps of all the basis materials at once using a technique like the least squares method. In the event of unequal counts in each bin, energy bin weighting schemes based on the CNR of the background region can be used to improve decomposition accuracies and reduce noise. It is known that the maximum likelihood method has many attractive qualities such as being consistent, at least asymptotically unbiased and at least asymptotically absolutely efficient. It is also known that under certain conditions (where the errors in each of the measurements is assumed to be independently random and Gaussian distributed around the true model and the standard deviations of each of the normal distributions is assumed to be equal for all data points) the least squares solution approaches the maximum likelihood one. However, the maximum likelihood method is generally applied to the raw data prior to reconstruction where the statistics can be accurately modeled as Poisson. Here we examine image domain

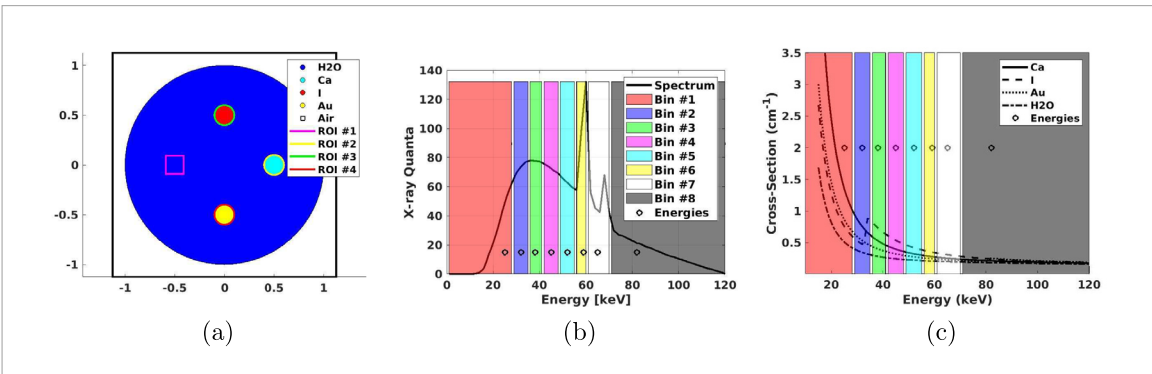


Figure 1. (a) Layout of materials for the four-material model. (b) $120\,\mathrm{kVp}\,x$ -ray source spectrum divided into eight equal count energy bins based on the flat field. The representative energies used in material decomposition are shown as open circles. These representative energies correspond to the median counts within each energy bin of the flat field spectrum divided into eight equal count energy bins. (c) Attenuation curves for calcium, iodine, gold and water with energy bins and representative energy values used to calculate the model linear attenuation coefficients used in material decomposition.

decomposition methods where the noise in the attenuation images has been significantly reduced due to the FBP reconstruction. We have found that this image noise is no longer Poisson making it difficult to select the proper model.

2.3. Multi-step material decomposition method

In a multi-step decomposition method, we propose that the material decomposition can now be computed in a series of steps, each separating one new material from the same multi-bin data. We describe the method with an example of a four-material decomposition. Successful results from six-material and mixed-material decompositions are shown in sections 2.9 and 2.10.

In our four-material model problem, the chosen materials are water, calcium, iodine and gold. Water represents the background breast tissue, calcium represents breast microcalcifications and gold and iodine are contrast agents. The model geometry is composed of a water background with columns of calcium, iodine and gold. Figure 1(a) shows a cross section of this phantom. In initial separation steps, the focus is examining how distinct the material is from the other materials based on the linear attenuation versus energy curves (Chantler 2000, 1995). In earlier steps, materials with similar attenuation properties can be grouped together to form a pseudo material. This pseudo material is modeled to have the average attenuation properties of the materials in the group. This step of forming pseudo material groups reduces the number of solution unknowns allowing for the separation of the most distinct material first. In this particular example, we virtually group calcium and gold together to form a pseudo material to first allow for the efficient separation of water which is the most abundant and lowest attenuating material. Next, the contrast agent materials can be separated due to their unique energy-dependent x-ray properties. Finally, the remaining materials can be separated in order of decreasing attenuation. In summary, when decomposing multi-material objects, we find that the following decomposition strategy consistently provides good results:

- 1. First, focus on accurately recovering the background or most abundant material using low energy bins.
- 2. Next, decompose materials with K-edges in the diagnostic range in order of decreasing attenuation using energy bins just higher in energy than these K-edge energies.
- 3. Next, decompose materials without K-edges in the diagnostic range in order of decreasing attenuation using low energy bins.

Equation (2) shows the first step of a multi-step decomposition for a four-material problem where the volume fraction of material 1 (water), $\vec{f_1}(\vec{r})$, is determined. The volume fraction of material 2 (iodine), $\vec{f_2}(\vec{r})$, and the volume fraction of the average of materials 3 and 4 (calcium and gold), $\vec{f_3}$, $4(\vec{r})$, are also determined in this step. However, this step is optimized in terms of energy bins used for the separation of material 1, so these other volume fractions are discarded. In equation (2), E_j represents the energy values used to calculate the model linear attenuation coefficients, $\mu_1(E_j)$, $\mu_2(E_j)$ and $\bar{\mu}_{3,4}(E_j)$, of materials 1, 2 and the average of 3 and 4, respectively.

$$\vec{\mu}(E_i, \vec{r}) = \mu_1(E_i)\vec{f_1}(\vec{r}) + \mu_2(E_i)\vec{f_2}(\vec{r}) + \bar{\mu}_{3,4}(E_i)\bar{\vec{f}_{3,4}}(\vec{r}). \tag{2}$$

In the second step, the K-edge agent of material 2 is separated from the remaining three-material mixture as represented in equation (3). The pseudo material with the average attenuation properties of materials 3 and 4 is maintained in this step as well.

$$\vec{\mu}(E_j, \vec{r}) - \mu_1(E_j)\vec{f_1}(\vec{r}) = \mu_2(E_j)\vec{f_2}(\vec{r}) + \bar{\mu}_{3,4}(E_j)\vec{\bar{f}}_{3,4}(\vec{r}). \tag{3}$$

In implementing the least squares solution to equation (3), one assumes the knowledge of material 1 obtained from step 1 as a prior information as shown on the left-hand side. The solution yields a map of material 2 and a map of the pseudo material for materials 3 and 4, which is discarded when proceeding to the next step. In step 3, we separate the next most attenuating material of material 3 from the remaining two-material mixture as represented in equation (4).

$$\vec{\mu}(E_j, \vec{r}) - \mu_1(E_j)\vec{f}_1(\vec{r}) - \mu_2(E_j)\vec{f}_2(\vec{r}) = \mu_3(E_j)\vec{f}_3(\vec{r}) + \mu_4(E_j)\vec{f}_4(\vec{r}). \tag{4}$$

In the final step, material 4 is refined to improve its decomposition accuracy as shown in equation (5).

$$\vec{\mu}(E_i, \vec{r}) - \mu_1(E_i)\vec{f_1}(\vec{r}) - \mu_2(E_i)\vec{f_2}(\vec{r}) - \mu_3(E_i)\vec{f_3}(\vec{r}) = \mu_4(E_i)\vec{f_4}(\vec{r}). \tag{5}$$

At each step, the respective equation (equations (2)–(4) or (5)) is solved using multiple energy bin data (j = 1, 2, ..., 8) collected via the initial, single acquisition with a PCD. This same original multi-bin data can be reformulated in later steps to reduce the number of bins and improve count statistics. Depending on the problem, a conservation of volume constraint indicating that the domain is comprised of only the known four materials can be included in each step of multi-step and single-step as described by equation (6) where i is the material index of the M total materials. With the addition of equation (6), the system of energy based equations (based on equations (2)–(4) or (5)) can be solved for material volume fractions using a bounded variable least squares approach.

$$\sum_{i}^{M} \vec{f}_i(\vec{r}) = 1. \tag{6}$$

In implementing this step-by-step approach, the system of equations solved in each step becomes smaller and better conditioned allowing for the accurate separation of more materials than conventional single-step techniques.

2.4. Energy bin selection strategy

In accordance with the itemized list shown in section 2.3 which provides a general formula for the multi-step strategy, the energy bins used in each step of the multi-step algorithm can be selected. We maintain the same material numbering scheme (1 = water, 2 = iodine, 3 = calcium and 4 = gold) and multi-step strategy as described in section 2.3. As displayed in figures 1(b), 2(b) and 3(b), the eight energy bins simulated for each of these example problems represent [1,28], [29,35], [36,41], [42,48], [49,55], [56,60], [61,70] and [71,120] keV, respectively. The representative energies corresponding to the median counts within each of these bins are [25,32,38,45,52,59,65,82] keV, respectively. These representative energies were used to determine the linear attenuation coefficients of the inversion matrices used in decomposition. Bin selection rules can follow general trends detailed here, but one must exclude bins with extremely low counts. As an example, for the current case, there is only one energy bin greater than the K-edge energy of gold. This high energy data was found to contain very little signal and mostly noise with CNRs of calcium and gold regions found to be less than 1 making them nearly invisible. Therefore, this data was not used in decomposition and gold was treated as a non-contrast agent material. In cases like this where there is no information and only noise and artifacts, we find that excluding these bins leads to a better decomposition. However for a different x-ray spectrum with sufficient signal in the highest energy bin, one might choose to use this bin.

For the example detailed above, in step 1, we use only bins 1–3 as there are three unknowns and material 1 has its highest contrast from the remaining materials at low energies. In step 2, we separate material 2 using bins 3 and 4 because these bins are just higher in energy than the K-edge (33.2 keV) where material 2 is the most distinguishable from the remaining materials. In step 3, we use bins 1 and 2 as there are two unknowns and material 2 has its highest contrast at low energies. In the final step, we use only bin 1 and ignore the K-edge of material 4 as we do not have low noise data for energies above this K-edge. This strategy worked well for the simulated phantoms described in this work, but is still an area of active research as we apply the method to CT data collected with a physical x-ray detector.

2.5. Contrast to noise ratio weighting

Energy bin weighting is performed in each step of the multi-step method to provide high accuracy decompositions with low noise. For any given step, the energy weighting factor is estimated from the CNR of the material under focus estimated for each energy bin. This is a benefit of the multi-step technique that is not possible in a single-step approach. Equation (7) displays the relationship for calculating the weights for each step based on the signal and background of the decomposed material where j represents the energy bin used for the calculation. In most

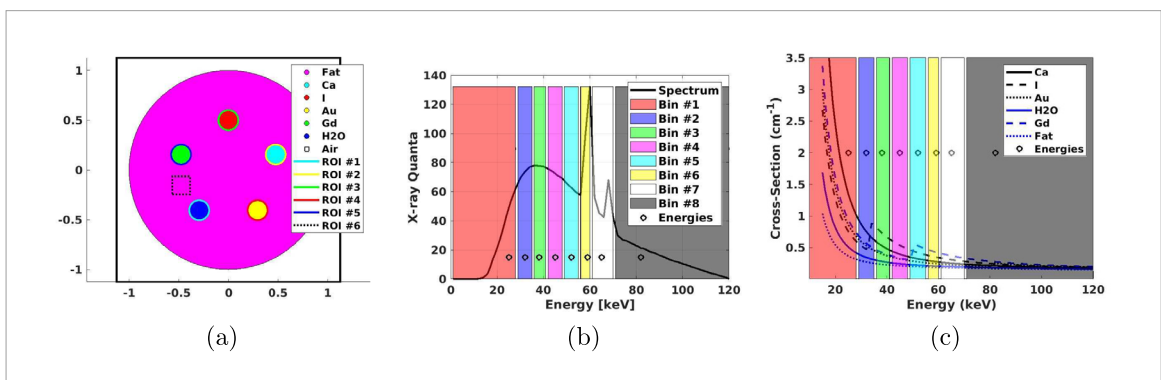


Figure 2. (a) Layout of materials for the six-material model. (b) 120 kVp x-ray source spectrum divided into eight equal count energy bins based on the flat field. The representative energies used in material decomposition are shown as open circles. These representative energies correspond to the median counts within each energy bin of the flat field spectrum divided into eight equal count energy bins. (c) Attenuation curves for calcium, iodine, gold, water, gadolinium and adipose with energy bins and representative energy values used to calculate the model linear attenuation coefficients used in material decomposition.

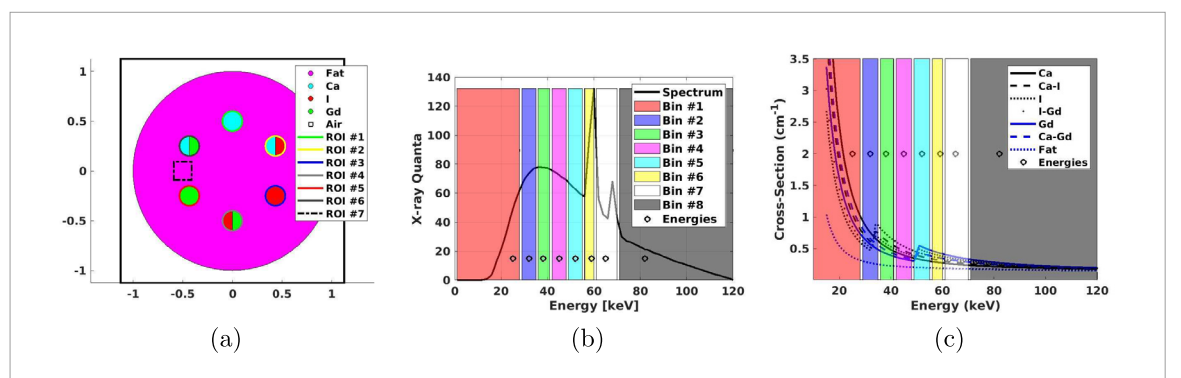


Figure 3. (a) Layout of materials for the four-material, mixed-materials model. In this image, the multi-color circles indicate a 50%/50% mixture by volume of the two materials that fills the entire well. It is not meant to indicate the spatial distribution of the two materials within the well. (b) 120 kVp x-ray source spectrum divided into eight equal count energy bins based on the flat field. The representative energies used in material decomposition are shown as open circles. These representative energies correspond to the median counts within each energy bin of the flat field spectrum divided into eight equal count energy bins. (c) Attenuation curves for calcium, calcium—iodine mixture, iodine, iodine—gadolinium mixture, gadolinium, calcium—gadolinium mixture and adipose with energy bins and representative energy values used to calculate the model linear attenuation coefficients used in material decomposition.

steps, $\mu_{signal,j}$ and $\sigma^2_{signal,j}$ are treated as the mean and variance in the attenuation in the small region occupied by the material under focus in that step (ROI#2, ROI#3 and ROI#4 for the four-material problem seen in figure 1(a), ROI#1, ROI#2, ROI#3, ROI#4 and ROI#5 for the six-material problem seen in figure 2(a) or ROI#1, ROI#3 and ROI#5 for the mixed-material problem seen in figure 3(a)) and $\mu_{background,j}$ and $\sigma^2_{background,j}$ are the mean and variance in the attenuation in the water or fat based on the primary material of the phantom cylinder. When decomposing the water or fat, $\mu_{signal,j}$ and $\sigma^2_{signal,j}$ are taken as the mean and variance in the water or fat and $\mu_{background,j}$ and $\sigma^2_{background,j}$ are taken as the mean and variance in the region surrounding the phantom. The entire water or fat region was used in the calculation of all weights. These CNRs form the diagonal elements of a weighting matrix which is applied to the inversion matrix and the attenuation data during the least squares solution.

$$CNR_{j} = \frac{\mu_{signal,j} - \mu_{background,j}}{\sqrt{\sigma_{signal,j}^{2} + \sigma_{background,j}^{2}}}.$$
(7)

In practice, these weights can be computed from calibration vials included in the field of view during the acquisition of the unknown decomposition phantom. ROIs selected within reconstructed slices of these calibration vials can be used to define CNR weights as well as calibrated basis functions for the decomposition of the unknown object.

2.6. Computational costs of the algorithms

All of the decompositions conducted in this work were run on an AMD 2.2 GHz CPU with 128 gigabytes of RAM and 32 available cores. Each decomposition was run in parallel on 16 cores using MATLAB 2016's parallel computing toolbox. The resulting computational times of each problem for both algorithms will be noted in the sections to follow.

2.7. Material map analysis

The material decomposition results were evaluated qualitatively and quantitatively. Quantitation was assessed based on three criteria: percent error, CNR and noise standard deviation (NSD). The relationship for calculating percent error can be seen in equation (8) where $f_{ROI,i}$ represents the mean volume fraction in region of interest (ROI) i and $f_{ROI,i,true}$ represents the true volume fraction in ROI i.

$$Error_{\text{ROI},i} = \frac{|f_{\text{ROI},i} - f_{\text{ROI},i,true}|}{f_{\text{ROI},i,true}} \times 100.$$
(8)

The relationship for calculating CNR can be seen in equation (9) where $\sigma_{ROI,i}^2$ represents the variance in the volume fractions in ROI i and $\sigma_{RestofImage}^2$ represents the variance in the volume fractions of the rest of the image. For the background region, only the square ROI seen in figures 1(a), 2(a) and 3(a) were used to calculate the mean and variance for ROI i, but the remaining background material region was excluded from the calculations of the mean and variance of the rest of the image.

$$CNR_{ROI,i} = \frac{f_{ROI,i} - f_{RestofImage}}{\sqrt{\sigma_{ROI,i}^2 + \sigma_{RestofImage}^2}}.$$
(9)

The relationship for calculating NSD can be seen in equation (10) where $\sigma_{ROI,i}$ is the standard deviation of the volume fractions in ROI *i*.

$$NSD_{ROI,i} = \sigma_{ROI,i} \times 100. \tag{10}$$

2.8. Four-material decomposition

The model geometry consists of a 2 cm diameter cylinder of water with 2 mm diameter columns of calcium, iodine and gold. The background is pure water and the concentrations of calcium, iodine and gold are $140 \,\mathrm{mg} \,\mathrm{ml}^{-1}$, $18 \,\mathrm{mg} \,\mathrm{ml}^{-1}$ and $8 \,\mathrm{mg} \,\mathrm{ml}^{-1}$, respectively. A diagram of the four-material problem can be seen in figure 1(a) along with the ROIs used in the analysis of the results. For comparison, the results of the new multi-step method will be compared with the results of the single-step method. The decomposition problem was solved with single-step in accordance with equation (1) and with multi-step in accordance with equations (2)–(5). For this problem, the background material water is material 1, iodine is material 2, calcium is material 3 and gold is material 4.

After each step of multi-step and single-step, a threshold was applied to reduce the impact of noise and improve the decomposition results. More aggressive threshold application is justified in the first step of multistep because this step decomposes the background which is assumed to be pure water with a uniform volume fraction of one. Less aggressive application of thresholds is performed on the other material maps to reduce the impact of noise. Thresholds of 0.25 and 0.75 were used for steps 2-4 of multi-step and for all material maps of single-step. A threshold of 0.6 was used for the first step of multi-step. Since the first step is to recover the most abundant background material, this threshold choice is somewhat flexible and the experimenter can opt for a value that eliminates most of the noise in regions with uniform composition. Not using these thresholds would slightly increase the noise and quantitative errors in both single-step and multi-step, but overall the multistep method still yields better results than single-step. Applying thresholds such as these has been suggested is other works for the elimination of low values in decomposed images due to noise in the attenuation data (Raja et al 2018). The application of thresholds has also been employed during the solution of some iterative methods for the elimination of eigenvalues attributed to noise only during singular value decomposition and to enforce sparsity of materials contained in each voxel (Ding et al 2018). We want to emphasize that thresholding works differently in the two methods (single-step versus multi-step). For single-step, thresholding is more of a postprocessing operation that can simply reduce noise in the resulting basis images. Again, this is because all results are obtained at once. In multi-step, the results from prior steps feed into succeeding steps. This makes thresholding more effective for multi-step and this ability is unique to the multi-step technique.

Figure 1 shows the energy bins chosen based on equal mean flat field counts overlaid on (b) the x-ray source spectrum and (c) linear attenuation curves for the four materials in this problem. The representative energies for each bin are also displayed as the open circles. These linear attenuation curves were generated based on the maximum concentrations expected in the sample. This knowledge would be available to the experimenter as they would know the base concentration injected into the patient. This kind of *a priori* information is essential to the success of most decomposition techniques as it reduces the solution space to a manageable set of likely solutions. All material maps generated during the multi-step material decomposition process can be seen in figure 4. A dramatic improvement in the decomposition of iodine can be seen between steps 1 (figure 4(b)) and 2 (figure 4(d)). This is due to the energy bins and bin weighting used in step 2 which are optimized for the decomposition of iodine. The energy bins and bin weighting used in step 1 are optimized for the decomposition of water; therefore, they do not provide the best results for iodine. A less dramatic improvement is seen in the gold region

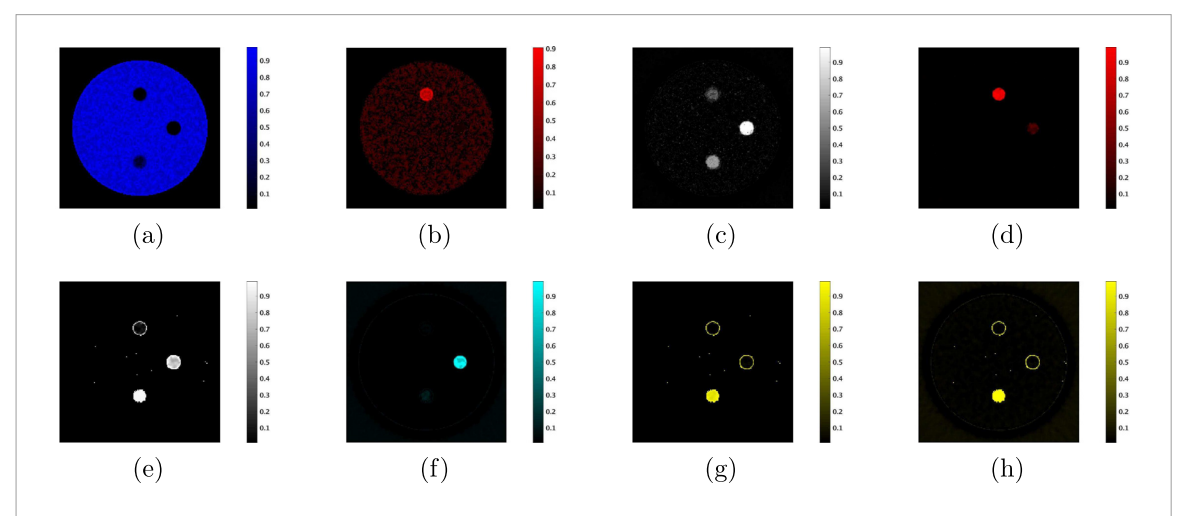


Figure 4. Material maps resulting from each step of multi-step material decomposition for the four-material problem. (a)–(c) are the water map (under focus), the iodine map (discarded) and the average of calcium and gold map (discarded) from step 1, respectively. (d) and (e) are the iodine map (under focus) and the average of calcium and gold map (discarded) from step 2, respectively. (f) and (g) are the calcium map (under focus) and the gold map (discarded) from step 3, respectively. (h) is the gold map (under focus) from step 4. These results correspond to the ground truth image shown in figure 5(a). The combined final results for multi-step can be seen in figure 5(c) and the quantitation can be seen in tables 1 and 2.

between steps 3 (figure 4(g)) and 4 (figure 4(h)). Again, the optimization of energy bins and bin weighting leads to better decomposition of gold in step 4 than step 3. Energy bin weighting based on the water region was conducted for the single-step results shown in figure 5(b) for the sake of comparison. The combined final results for the four-material problem for single-step and multi-step can be seen in figure 5 and the quantitation can be seen in tables 1 and 2. The multi-step method clearly outperforms the single-step method. This can be seen in the gold region in figure 5 and in the percent errors in table 1. The percent error is 70.3% for single-step versus 7.8% for multi-step. By examining the images in figure 5 and the CNRs in table 2, we can see an improvement in noise, especially in the water region. This is evidenced by a CNR of 20.8 for single-step versus 32.9 for multi-step. Also, the weighted matrices of linear attenuation coefficients for the four-material problem do indeed become better conditioned as the condition numbers are 21 161 for single-step versus 152, 134, 73 and 1 for the four consecutive steps of the multi-step method. The computational times in seconds for single-step and multi-step for the four-material problem are 93.3 and 235.5, respectively.

2.9. Six-material decomposition

A six-material case was chosen to display the ability of the method to handle more challenging decomposition problems. Here, gadolinium and adipose are added to the model. Gadolinium is another contrast agent with a K-edge. Adipose is a low contrast material significant to the breast imaging problem. In this problem, the background was adipose and water was made one of the columns. The adipose background was 2 cm in diameter and the columns of all other materials were 2 mm in diameter. The concentration of gadolinium was $18 \,\mathrm{mg}\,\mathrm{ml}^{-1}$. The adipose material properties were collected from ICRU-44 (White et al 1989). A diagram of this sixmaterial problem can be seen in figure 2(a) along with the ROIs used to compute the quantitative results. A similar approach of decomposing the background first, followed by the contrast agents and then the remaining materials was taken to achieve the goal of accurate separation of all six materials. A description of the material maps acquired in each step of multi-step material decomposition for the six-material problem along with the energy bins used can be seen in the flowchart in figure 6. The materials are decomposed in the following order: (1) adipose, (2) iodine, (3) gadolinium, (4) calcium, (5) gold and (6) water. In early steps, iodine and gadolinium are grouped together and calcium, gold and water are grouped together to reduce the number of unknowns and provide a better conditioned system of equations. Examination of the attenuation curves for these six materials, shown in figure 2(c), justifies the order that we separate materials and the energy bins used in each step. In the first step, we have three unknowns and the most distinct material, adipose, has its highest contrast from the other materials at low energies. For this reason, we choose the three lowest energy bins. In the second step, we separate iodine which has its highest contrast for energy values slightly above its K-edge. For this reason, we choose bins 3–5 for step 2. Gadolinium has its highest contrast above its K-edge, so we choose bins 6 and 7 for step 3. There are only two unknowns in step 3, so we choose only two energy bins. Calcium is the highest attenuating material of the remaining materials and its contrast is highest at low energies, so we use bins 1 and 2 for step 4. Gold is the next most attenuating material and has its highest contrast at low energies, so we again choose bins 1 and 2 for this step. Finally, we choose bin 1 for water as it is the lowest attenuating material with maximum contrast at low energies. The same conservation of volume constraint seen in equation (6) was applied to each step of the six-material

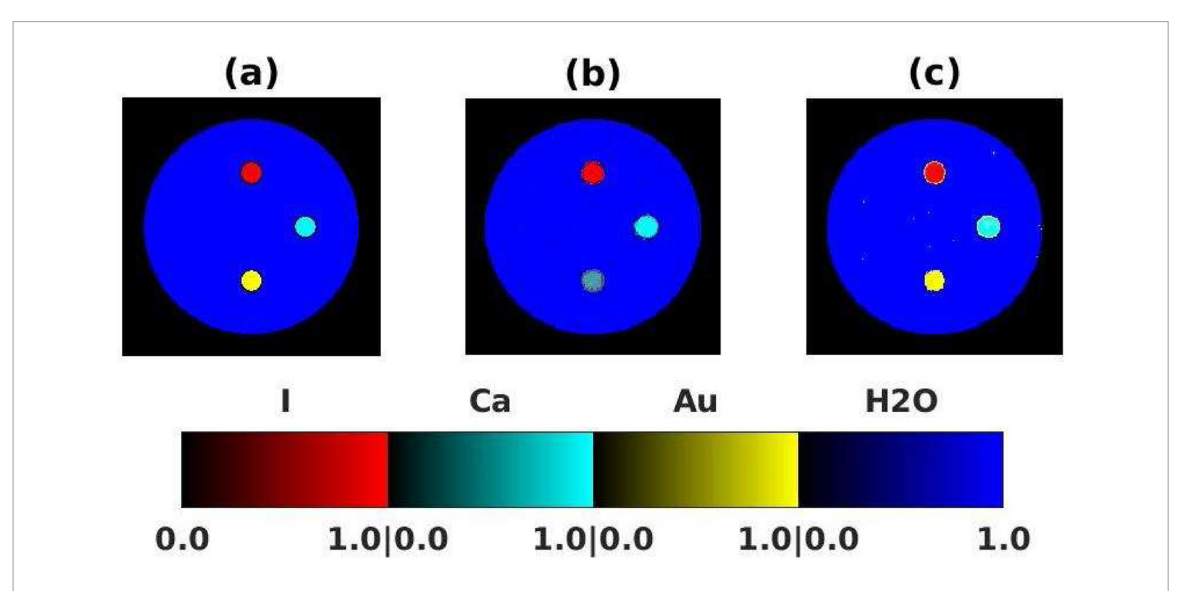


Figure 5. Color coded (a) ground truth, (b) single-step decomposition results and (c) multi-step decomposition results for the four-material problem.

Table 1. Percent errors in the calculated volume fractions of each ROI (ROI#1, ROI#2, ROI#3, ROI#4) for each material map generated using the single-step and multi-step material decomposition techniques. The bold values are of most interest as these represent the percent errors in a material ROI in its respective map.

	Single-step	Multi-step
Water map	0.2 , 0.1, 1.6, 37.4	0.0 , 0.0, 0.0, 7.8
Calcium map	0.0, 5.6 , 0.0, 22.9	0.0, 6.4 , 0.0, 0.0
Iodine map	0.0, 0.0, 8.3 , 0.0	0.0, 8.9, 11.7, 0.0
Gold map	0.0, 3.1, 0.5, 70.3	0.0, 6.3, 11.2, 7.8

Table 2. Contrast to noise ratios (CNRs) and NSDs in percent in each ROI (ROI#1, ROI#2, ROI#3, ROI#4) for each material map generated using the single-step and multi-step material decomposition techniques. The bold values are of most interest as these represent the CNRs and NSDs in a material ROI in its respective map.

	Single-step		Multi-step	
	CNR	NSD	CNR	NSD
Water map	20.8	2.3 , 1.8, 7.5, 5.7	32.9	0.0 , 0.0, 0.0, 26.9
Calcium map	6.6	0.0, 14.0 , 0.0, 13.6	5.8	0.0, 16.0 , 0.0, 0.0
Iodine map	5.2	0.0, 0.0, 17.5, 0.0	3.5	0.0, 13.9, 25.0 , 0.0
Gold map	12.8	0.0, 9.0, 3.5, 1.3	3.4	0.0, 16.2, 24.1, 26.9

problem. Bounded variable least squares was again used to solve this inverse problem. Bounds of zero and one were applied to all of the unknowns. Thresholds were again applied after each step of the multi-step process and to the single-step results used for comparison. A threshold of 0.85 was used for the first step of multi-step and thresholds of 0.25 and 0.75 were applied to all other steps of multi-step and to all material maps of single-step.

All material maps generated during the multi-step material decomposition process can be seen in figure 7. A dramatic improvement in the decomposition of gadolinium can be seen between steps 2 (figure 7(e)) and 3 (figure 7(g)). This is due to the energy bins and bin weighting used in step 3 which are optimized for the decomposition of gadolinium. The energy bins and bin weighting used in step 2 are optimized for the decomposition of iodine; therefore, they do not yield the best results for gadolinium. No improvement is seen in the water region between steps 5 (figure 7(l)) and 6 (figure 7(m)) because there is already zero error in the water region after step 5. Some improvement is expected if error did exist in the water region after step 5 and it is recommended to maintain refinement step 6. Energy bin weighting based on the adipose region was conducted for the single-step results shown in figure 8(b). The combined final results for the six-material problem for single-step and multi-step can be seen in figure 8 and the quantitation can be seen in tables 3 and 4. It is also clear for the six-material case that the multi-step method outperforms the single-step method. This can be seen in nearly all regions in figure 8 and in the percent errors in table 3. For example, the percent error for water is 64.4% for single-step versus 7.2% for multi-step. The percent error for adipose is 39.8% for single-step versus 2.5% for multi-step. The six-

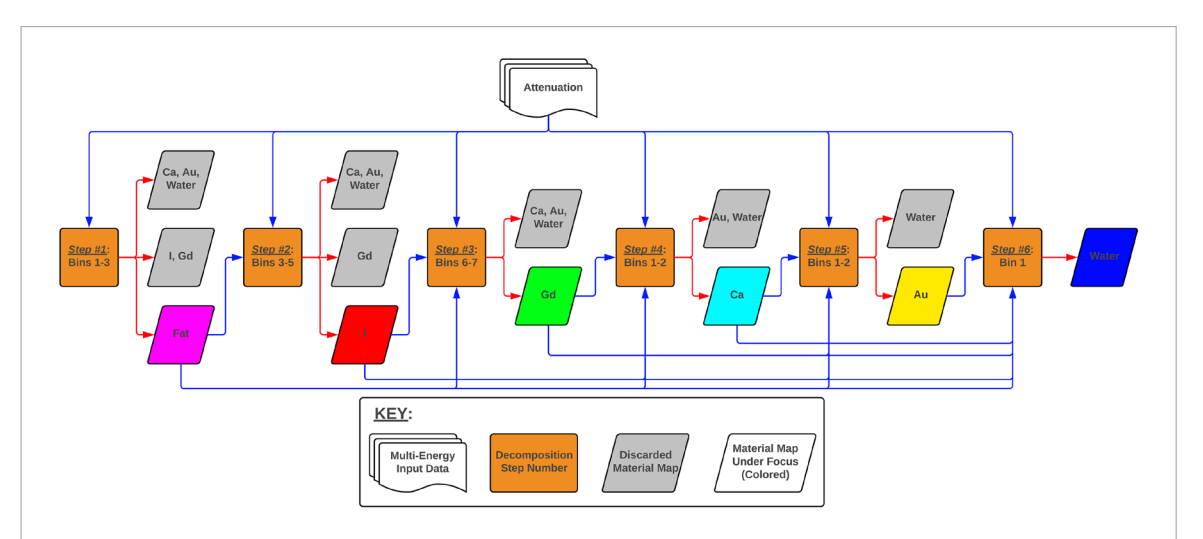


Figure 6. Flowchart describing the steps of a multi-step material decomposition for the six-material problem. Blue arrows indicate inputs to decomposition steps and red arrows indicate outputs of decomposition steps. The key describing the inputs, outputs and steps of the decomposition can be seen above. The discarded material maps labeled with multiple materials represent a single pseudo material map representing the average of the group. The colored material maps represent the material under focus during the current decomposition step which are maintained throughout the process as final results.

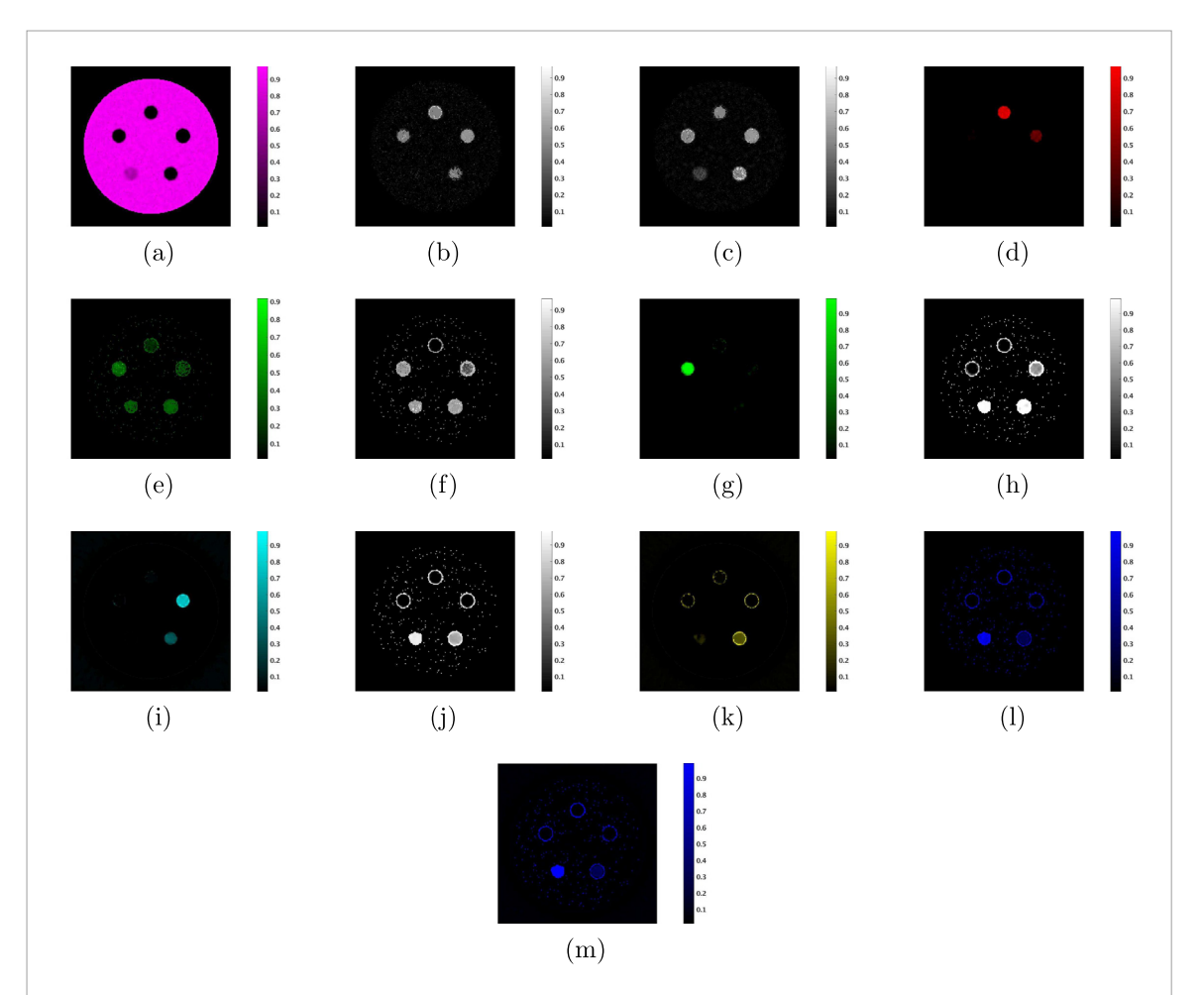


Figure 7. Material maps resulting from each step of multi-step material decomposition for the six-material problem. (a)—(c) are the adipose map (under focus), the average of iodine and gadolinium map (discarded) and the average of calcium, gold and water map (discarded) from step 1, respectively. (d)—(f) are the iodine map (under focus), the gadolinium map (discarded) and the average of calcium, gold and water map (discarded) from step 2, respectively. (g) and (h) are the gadolinium map (under focus) and the average of calcium, gold and water map (discarded) from step 3, respectively. (i) and (j) are the calcium map (under focus) and the average of gold and water map (discarded) from step 4, respectively. (k) and (l) are the gold map (under focus) and the water map (discarded) from step 5, respectively. (m) is the water map (under focus) from step 6. The results shown here correspond to the ground truth image shown in figure 8(a). The combined final results for multi-step can be seen in figure 8(c) and the quantitation can be seen in tables 3 and 4.

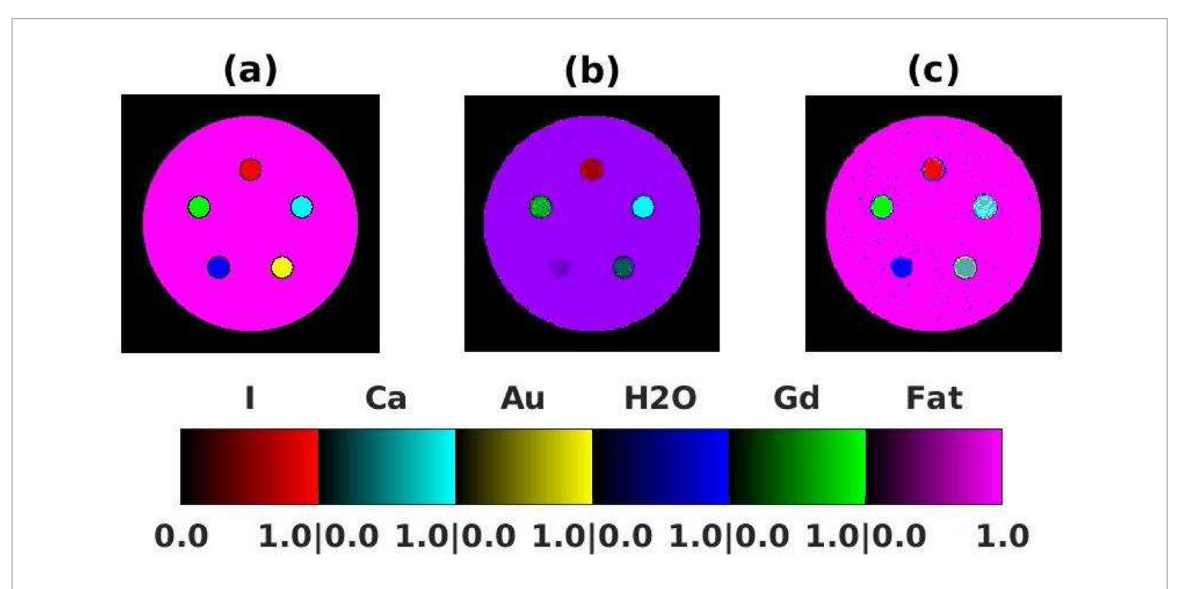


Figure 8. Color coded (a) ground truth, (b) single-step decomposition results and (c) multi-step decomposition results for the six-material problem.

Table 3. Percent errors in the calculated volume fractions of each ROI (ROI#1, ROI#2, ROI#3, ROI#4, ROI#5, ROI#6) for each material map generated using the single-step and multi-step material decomposition techniques. The bold values are of most interest as these represent the percent errors in a material ROI in its respective map.

Single-step	Multi-step
64.4 , 0.0, 0.0, 2.3, 0.0, 38.7	7.2 , 4.2, 6.2, 30.2, 3.9, 2.5
0.0, 6.4 , 0.1, 28.9, 10.3, 0.0	0.0, 15.8 , 0.0, 25.4, 0.1, 0.0
0.0, 0.0, 34.9 , 0.0, 0.0, 0.0	0.0, 28.9, 12.3 , 0.0, 0.0, 0.0
0.0, 0.1, 0.0, 99.4 , 0.0, 0.0	0.0, 1.3, 4.7, 55.2 , 6.1, 0.0
0.0, 0.0, 0.0, 0.0, 46.3 , 0.0	0.0, 0.0, 0.7, 0.0, 10.6 , 0.0
47.8, 0.0, 0.5, 3.5, 0.6, 39.8	7.2, 0.0, 0.0, 0.0, 0.0, 2.5
	64.4, 0.0, 0.0, 2.3, 0.0, 38.7 0.0, 6.4, 0.1, 28.9, 10.3, 0.0 0.0, 0.0, 34.9, 0.0, 0.0, 0.0 0.0, 0.1, 0.0, 99.4, 0.0, 0.0 0.0, 0.0, 0.0, 0.0, 46.3, 0.0

Table 4. Contrast to noise ratios (CNRs) and NSDs in percent in each ROI (ROI#1, ROI#2, ROI#3, ROI#4, ROI#5, ROI#6) for each material map generated using the single-step and multi-step material decomposition techniques. The bold values are of most interest as these represent the CNRs and NSDs in a material ROI in its respective map.

	Single-step		Multi-step	
	CNR	NSD	CNR	NSD
Water map	0.8	1.7 , 0.0, 0.0, 7.6, 0.0, 1.5	3.2	26.0 , 11.2, 18.0, 13.4, 13.3, 15.6
Calcium map	5.7	0.0, 16.2 , 2.0, 12.6, 14.3, 0.0	5.0	0.0, 16.8 , 0.0, 14.3, 2.0, 0.0
Iodine map	4.7	0.0, 0.0, 14.0 , 0.0, 0.0, 0.0	3.6	0.0, 16.4, 24.5 , 0.0, 0.0, 0.0
Gold map	0.2	0.0, 1.8, 0.0, 3.8 , 0.0, 0.0	1.9	0.0, 5.9, 11.8, 23.8 , 14.2, 0.0
Gadolinium map	2.7	0.0, 0.0, 0.0, 0.0, 20.0 , 0.0	4.3	0.0, 0.0, 4.5, 0.0, 20.6 , 0.0
Adipose map	10.7	3.1, 0.0, 3.8, 9.6, 4.1, 1.6	6.1	26.0, 0.0, 0.0, 0.0, 0.0, 15.6

material case also displays similar noise properties for the two methods as evidenced by figure 8 and the CNRs in table 4. This is evidenced by an average CNR of the six material regions of 4.1 for single-step versus 4.0 for multistep. And again, the weighted matrices of linear attenuation coefficients for the six-material problem become better conditioned as the condition numbers are 9737 867 for single-step versus 669, 403, 183, 37, 86 and 1 for the six consecutive steps of multi-step. The computational times in seconds for single-step and multi-step for the six-material problem are 97.2 and 288.2, respectively.

2.10. Four-material, mixed-material decomposition

To display the ability of the multi-step method to handle a problem where different materials are mixed together in different concentrations, we show a four-material, mixed material problem. In this problem, there are six contrast elements embedded in an adipose background as shown in the ground truth image in figure 3(a). Starting from the top material and working around the circular array clockwise the mixtures are: 140 mg ml⁻¹ calcium in water, 70 mg ml⁻¹ calcium/9 mg ml⁻¹ iodine in water, 18 mg ml⁻¹ iodine in water, 9 mg ml⁻¹

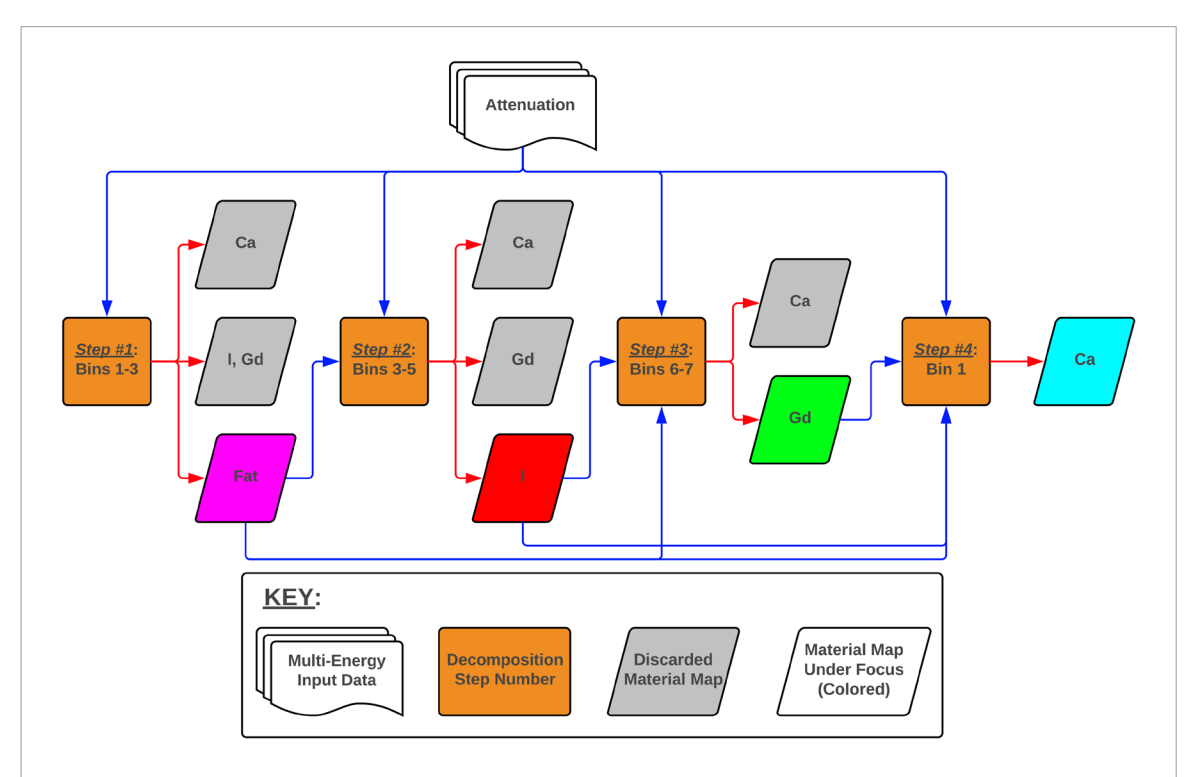


Figure 9. Flowchart describing the steps of a multi-step material decomposition for the four-material, mixed-materials problem. Blue arrows indicate inputs to decomposition steps and red arrows indicate outputs of decomposition steps. The key describing the inputs, outputs and steps of the decomposition can be seen above. The discarded material maps labeled with multiple materials represent a single pseudo material map representing the average of the group. The colored material maps represent the material under focus during the current decomposition step which are maintained throughout the process as final results.

iodine/9 mg ml⁻¹ gadolinium in water, 18 mg ml⁻¹ gadolinium in water and 70 mg ml⁻¹ calcium/9 mg ml⁻¹ gadolinium in water. The adipose material properties were again collected from ICRU-44 (White et al 1989). The corresponding 120 kVp spectrum and linear attenuation curves for these materials are shown in figures 3(b) and (c). Similar to the six-material problem the materials were decomposed in the following order: (1) adipose, (2) iodine, (3) gadolinium and (4) calcium. A description of the steps of the multi-step method and energy bins used at each step for the four-material, mixed-material problem are shown in figure 9. The maximum concentrations of calcium, iodine and gadolinium mentioned above were used as basis functions and weighting based on the CNRs of these material regions were used during the weighted least squares solution. Since similar materials and concentrations to the six-material problem were used in this mixed-material problem, a similar decomposition strategy was employed. The three groups of the background, the contrast agents with K-edges and the noncontrast agents were maintained in this problem as well. Energy bins were again selected to maximized contrast between the focus material and the remaining, undecomposed materials. The same conservation of volume constraint seen in equation (6) was applied to each step of this mixed-material problem. Bounded variable least squares was used to solve this inverse problem. Bounds of zero and one were applied to all of the unknowns. A threshold of 0.6 was applied to the adipose map after the first step of the multi-step process and thresholds of 0.25 and 0.75 were applied to the adipose map of the single-step results used for comparison. No other thresholds were applied during the solution of other steps of the multi-step method or to any of the other maps of singlestep.

All material maps generated during the multi-step material decomposition process can be seen in figure 10. A dramatic improvement in the decomposition of gadolinium can be seen between steps 2 (figure 10(e)) and 3 (figure 10(g)). Similar to the 6-material problem, the energy bins and bin weighting used in step 3 are optimized for the decomposition of gadolinium. The energy bins and bin weighting used in step 2 are optimized for the decomposition of iodine; therefore, they do not yield the best results for gadolinium. Improvement is also seen in the calcium regions from earlier steps 1–3 (figures 10(c),(f) and (h)) and 4 (figure 10(i)) because optimal weighting for calcium is only conducted in step 4. Energy bin weighting based on the adipose region was conducted for the single-step results shown in figure 11(b). The combined final results for the four-material, mixed-material problem for single-step and multi-step can be seen in figure 11 and the quantitation can be seen in tables 5–7. It is also clear for this mixed-material case that the multi-step method outperforms the single-step method. This can be seen in the calcium and gadolinium regions which are incorrectly identified in the single-step method, but correctly identified in the multi-step method as shown in figure 11 and in the percent errors in table 5. Out

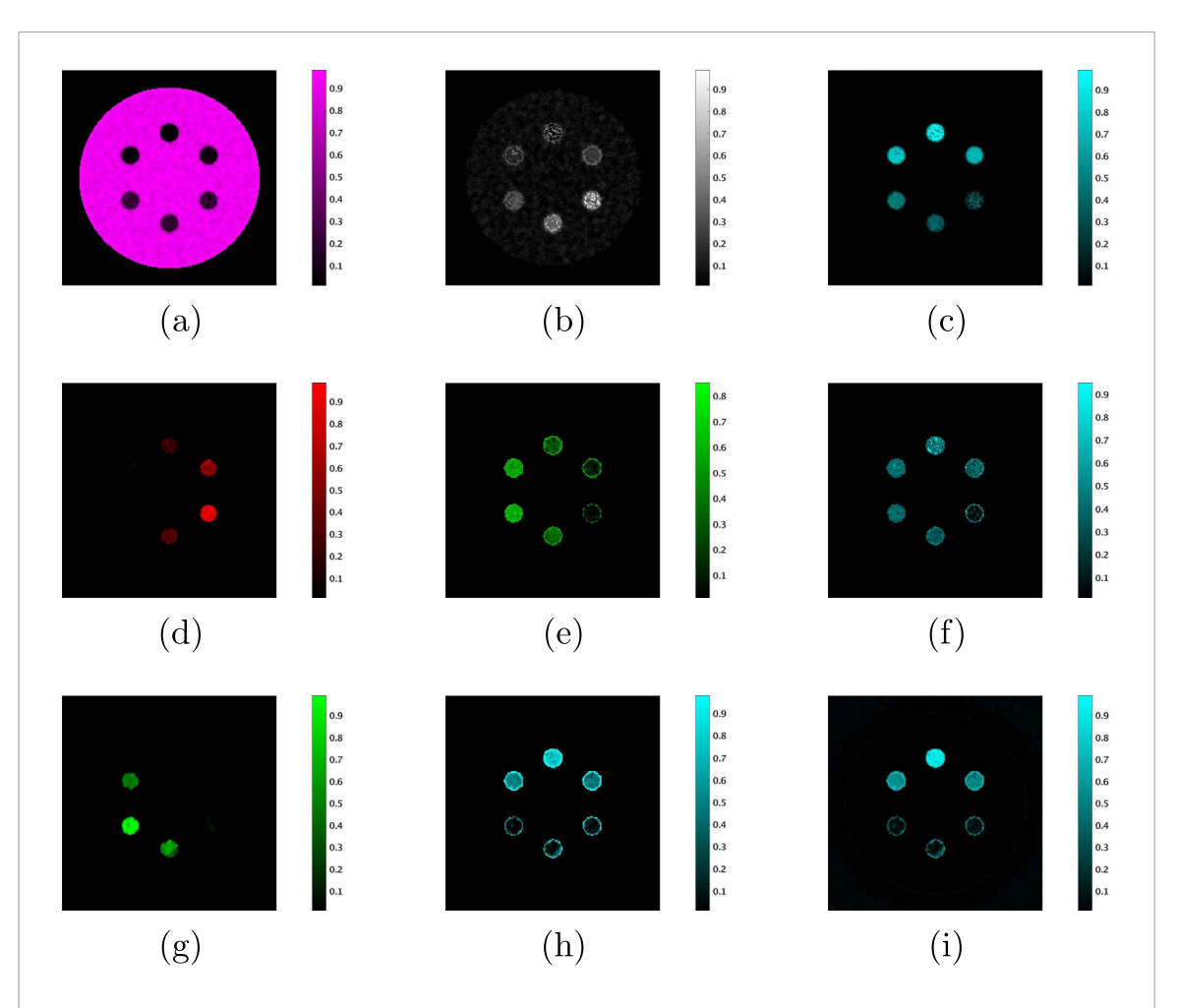


Figure 10. Material maps resulting from each step of multi-step material decomposition for the four-material, mixed-materials problem. (a)—(c) are the adipose map (under focus), the average of iodine and gadolinium map (discarded) and the calcium map (discarded) from step 1, respectively. (d)—(f) are the iodine map (under focus), the gadolinium map (discarded) and the calcium map (discarded) from step 2, respectively. (g) and (h) are the gadolinium map (under focus) and the calcium map (discarded) from step 3, respectively. (i) is the calcium map (under focus) from step 4. These results correspond to the ground truth image shown in figure 11(a). The combined final results for multi-step can be seen in figure 11(c) and the quantitation can be seen in tables 5-7.

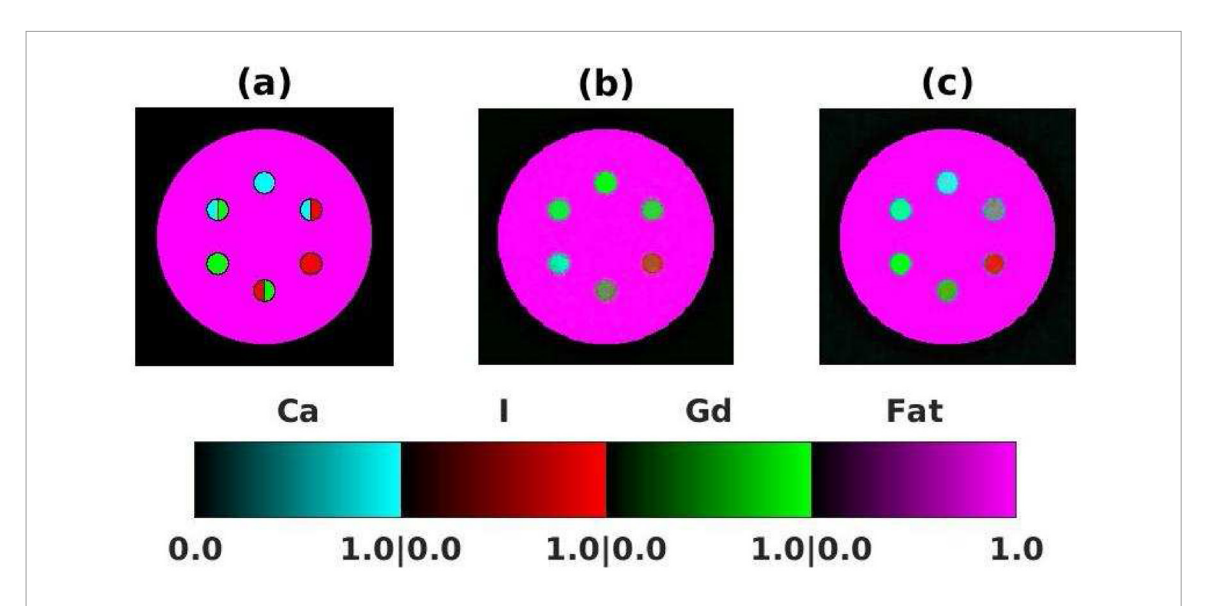


Figure 11. Color coded (a) ground truth, (b) single-step decomposition results and (c) multi-step decomposition results for the four-material, mixed-materials problem.

 $\textbf{Table 5.} \ \ Percent errors in the calculated volume fractions of each ROI (ROI\#1, ROI\#2, ROI\#3, ROI\#4, ROI\#5, ROI\#6, ROI\#7) for each material map generated using the single-step and multi-step material decomposition techniques. The bold values are of most interest as these represent the percent errors in a material ROI in its respective map.$

	Single-step	Multi-step
Adipose map	1.6, 3.4, 4.5, 5.4, 8.1, 4.6, 0.0	0.0, 0.0, 0.0, 0.5, 0.4, 0.0, 0.0
Calcium map	9.2 , 1.7 , 11.8, 19.8, 23.4, 13.1 , 0.3	10.5 , 4.6 , 16.4, 19.3, 14.4, 9.7 , 1.1
Iodine map	0.2, 30.4 , 33.0 , 11.8 , 2.3, 5.2, 4.7	17.4, 5.9 , 25.0 , 24.2 , 1.1, 2.3, 1.0
Gadolinium map	6.6, 23.6, 15.1, 18.7 , 40.6 , 26.6 , 1.7	1.4, 1.5, 3.2, 1.3 , 17.2 , 11.8 , 1.0

Table 6. Contrast to noise ratios (CNRs) in the form CNR (ROI#) that correspond to a particular material in its respective material map generated using the single-step and multi-step material decomposition techniques. The ROI# listed next to each CNR and the rest of the image not containing the material of interest are used to calculate the CNR for each material region in accordance with equation (9).

	Single-step	Multi-step
Adipose map	28.5 (#7)	97.6 (#7)
Calcium map	6.4 (#1), 4.9 (#2), 5.0 (#6)	12.0 (#1), 5.1 (#2), 6.3 (#6)
Iodine map	3.6 (#2), 5.4 (#3), 4.6 (#4)	2.2 (#2), 2.9 (#3), 2.0 (#4)
Gadolinium map	5.5 (#4), 3.3 (#5), 6.1 (#6)	2.7 (#4), 3.5 (#5), 2.3 (#6)

Table 7. Noise standard deviations (NSDs) in percent in each ROI (ROI#1, ROI#2, ROI#3, ROI#4, ROI#5, ROI#6, ROI#7) for each material map generated using the single-step and multi-step material decomposition techniques. The bold values are of most interest as these represent the NSDs in a material ROI in its respective map.

	Single-step	Multi-step
Adipose map	7.2, 10.6, 12.1, 13.1, 16.8, 12.2, 0.0	0.0, 0.0, 0.0, 6.8, 6.7, 0.0, 0.0
Calcium map	13.7 , 9.9 , 5.1, 5.2, 7.1, 12.3 , 0.8	5.6 , 9.5 , 14.7, 16.2, 13.7, 8.1 , 0.3
Iodine map	1.1, 3.8 , 11.5 , 7.2 , 4.5, 3.7, 1.7	11.0, 19.4 , 25.4 , 12.1 , 0.6, 2.8, 0.0
Gadolinium map	5.6, 2.9, 3.8, 5.2 , 17.6 , 3.0 , 1.0	1.5, 1.6, 3.9, 17.4 , 23.2 , 16.1 , 0.0

of the ten most significant regions (shown in bold in table 5), six show a decrease in error, one remains the same and three show an increase in error from single-step to multi-step. The mixed-material case also displays a similar improvement in noise as evidenced by figure 11 and the CNRs in table 6. This is evidenced by an increase in CNR in the adipose region for multi-step over the single-step baseline. In this case, the weighted matrices of linear attenuation coefficients for the mixed-material problem remain similarly conditioned as the condition numbers are 577 for single-step versus 549,988, 297, and 1 for the four consecutive steps of multi-step. The computational times in seconds for single-step and multi-step for this mixed-material problem are 92.5 and 237.7, respectively.

3. Discussion and conclusion

The proposed multi-step material decomposition method is demonstrated using simulated spectral CT images. We have shown decomposition of up to six materials with superior results in comparison to a conventional single step decomposition method and excellent preliminary experimental results (Fredette *et al* 2019). We have also shown the ability of the method to handle a four-material problem with mixed-materials and multiple concentrations. As shown here, performing the decomposition in multiple steps allows for flexibility in bin selection for each step where bins can be chosen to maximize quantitative accuracy for the material under focus in that step. Energy bins of the original data can be combined in several ways throughout the multi-step process to improve photon economy. Preferential bin weighting can also be performed to maximize contrast between the material being decomposed and the remaining materials in the mixture. The quantitative maps have been obtained in terms of volume fractions of each material in a given voxel. Formulating the problem in this manner allows for setting convenient bounds of zero and one for all variables in the bounded least squares solution. This technique also allows for the addition of a conservation of volume constraint that can be applied to certain problems to help stabilize the solution.

The bin selection rules for single and multi-step decomposition are currently being investigated. Generally, one must select at least as many bins as unknowns in the current decomposition step. When decomposing materials with K-edges, it is important to select energy bins above the K-edge energy of the material where contrast is maximized between the agent and the remaining materials. When decomposing materials without K-edges, selecting lower energy bins where contrast between the materials is maximized provides the best separation. We have also found that selectively applying the conservation of volume constraint during the decomposition of low

contrast materials and not during the decomposition of high contrast materials provides better decompositions. This has also been mentioned by others Bateman *et al* (2018).

Some simplifying assumptions have been used in this simulation framework. The effects of beam hardening, spectral distortions and scattering can cause the measured attenuation of an object to differ from expectation resulting in decomposition errors. The effects of beam hardening and scatter are negligible for the size of samples used in this study. For larger objects, corrections for these should be accounted for. Our simulation uses an ideal photon counting detector. In practice, quantitative inaccuracies could result from spectral distortions such as pulse pileup, k-escape and charge sharing. These inaccuracies in the measured energy distribution of photons can be overcome by various attenuation calibration or spectral correction techniques.

Pre-reconstruction and post-reconstruction filtering has been included prior to decomposition. Here we have chosen a two-dimensional Wiener filter because it is a statistical filter used to reduce additive noise. It was found through experimentation that small kernel sizes of 3×3 and 5×5 successfully minimized decomposition errors attributed to Poisson noise while minimally smoothing the boundaries between materials. Again, Vieira *et al* (2013) has shown that a Wiener filter can effectively reduce noise in both projections and reconstructions while maintaining small signals such as microcalcifications. Similar but slightly worse decomposition errors were seen with data filtered using a small kernel median filter, but errors increased more rapidly with increasing kernel size. As optimal filtering was not the primary focus of this work, only these two spatial domain filters were investigated and other options such as joint bilateral filtration may yield better decomposition results.

The idea of performing material decomposition in multiple steps is novel and versatile. We have demonstrated the multi-step method in image domain, but it could also be applied in projection domain. Overall, the percent errors, CNRs and NSDs of the multi-step method are similar to other studies (Le et al 2011, Le and Molloi 2011, Alessio and MacDonald 2013, Xue et al 2017) and the possibility to decompose up to six materials has been demonstrated. Most other methods that display the ability to decompose six materials, such as the ones by Xue et al (2017) and Ding et al (2018), use complex statistical techniques requiring high computational time. We believe that our simple and robust multi-step decomposition method is computationally efficient and suitable for a range of decomposition problems involving complex imaging tasks with several materials. Combining statistical iterative methods with our multi-step technique have the potential for enhanced results with larger number of materials. Further investigations which test the method with a bench top experimental system are ongoing. While the method is shown for data from a photon counting detector, it can be generally applied to data from multi-bin acquisition methods (such as an extension of dual energy imaging) without a photon counting detector as well.

Acknowledgments

This work was partially supported by funding from the US Department of Defense (DOD) Congressionally Directed Medical Research Program (CDMRP) Breakthrough Award BC151607 and the National Science Foundation CAREER Award 1652892.

References

Alessio A M and MacDonald L R 2013 Quantitative material characterization from multi-energy photon counting CT *Med. Phys.* 40 1–8 Alvarez R E and Macovski A 1976 Energy-selective reconstructions in x-ray computerized tomography *Phys. Med. Biol.* 21 733–44 Ballabriga R *et al* 2013 The Medipix3RX: a high resolution, zero dead-time pixel detector readout chip allowing spectroscopic imaging *IINST* 8 1–15

Barber R F, Sidky E Y, Schmidt T G and Pan X 2016 An algorithm for constrained one-step inversion of spectral CT data *Phys. Med. Biol.* 61 3784–818

Bateman CJ et al 2018 MARS-MD: rejection based image domain material decomposition JINST 13 1-13

Brooks R 1977 A quantitative theory of the Houndsfield unit and its application to dual energy scanning *J. Comput. Assist. Tomogr.* 1487–93 Cai C, Rodet T, Legoupil S and Mohammad-Djafari A 2013 A full-spectral Bayesian reconstruction approach based on the material decomposition model applied in dual-energy computed tomography *Med. Phys.* 40 111916

Chantler C 1995 Theoretical form factor, attenuation and scattering tabulation for z=1–92 from e=1–10 eV to e=0.4–1.0 meV *J. Phys. Chem. Ref. Data* **24** 71–643

Chantler C 2000 Detailed tabulation of atomic form factors, photoelectric absorption and scattering cross section, and mass attenuation coefficients in the vicinity of absorption edges in the soft x-ray (z=30-36, z=60-89, e=0.1 keV-10 keV), addressing convergence issues of earlier work *J. Phys. Chem. Ref. Data* **29** 597-1048

Chung J, Nagy J G and Sechopoulos I 2010 Numerical algorithms for polyenergetic digital breast tomosynthesis reconstruction SIAM J. Imaging Sci. 3 133–52

Coleman T and Li Y 1996 A reflective Newton method for minimizing a quadratic function subject to bounds on some of the variables SAIM J. Optim. 6 1040–58

Das M, Gifford H, O'Connor J and Glick S 2011 Penalized maximum likelihood reconstruction for improved microcalcification detection in breast tomosysothesis *IEEE Trans. Med. Imaging* 30 904–14

Ding Q, Niu T, Zhang X and Long Y 2018 Image-domain multi-material decomposition for dual-energy CT based on prior information of material images *Med. Phys.* 45 3614–26

Fredette N, Kavuri A and Das M 2018 A sensitivity analysis on parameters that affect a multi-step material decomposition for spectral CT *Proc. SPIE* 10573 105734K

Fredette N, Lewis C and Das M 2017 A multi-step method for material decomposition in spectral computed tomography *Proc. SPIE* 10132 101321C1-7

Fredette N, Vespucci S and Das M 2019 Experimental validation of a multi-step material decomposition for spectral CT *Proc. SPIE* 10948 109482T

Granton P V, Pollman S I, Ford N L, Drangova M and Holdsworth D W 2008 Implementation of dual- and triple-energy cone-beam micro-CT for postreconstruction material decomposition *Med. Phys.* 35 5030–42

Jakubek J, Jakubek M, Platkevic M, Soukup P, Turecek D, Sykora V and Vavrik D 2014 Large area pixel detector WIDEPIX with full area sensitivity composed of 100 Timepix assemblies with edgeless sensors JINST 9 C04018

Kalluri K S, Mahd M and Glick S J 2013 Investigation of energy weighting using an energy discriminating photon counting detector for breast CT Med. Phys. 40 0819231

Kappler S, Henning A, Krauss B, Schoeck F, Stierstorfer K, Weidinger T and Flohr T 2013 Multi-energy performance of a research prototype CT scanner with small-pixel counting detector *Proc. SPIE* 8668 86680O

Koenig T et al 2014 How spectroscopic x-ray imaging benefits from inter-pixel communication Phys. Med. Biol. 59 6195–213

Le HQ and Molloi S 2011 Least squares parameter estimation methods for material decomposition with energy discriminating detectors Med. Phys. 38 245–55

Le H Q and Molloi S 2011 Segmentation and quantification of materials with energy discriminating computed tomography: a phantom study *Med. Phys.* 38 228–37

Lee S, Choi Y and Kim H 2014 Quantitative material decomposition using spectral computed tomography with an energy-resolved photoncounting detector *Phys. Med. Biol.* 59 5457–82

Li Z, Leng S, Yu L, Yu Z and McCollough C H 2015 Image-based material decomposition with a general volume constraint for photon-counting CT Proc. SPIE 9412 94120T

Liu X, Yu L, Primak A and McCollough C 2009 Quantitative imaging of element composition and mass fraction using dual-energy CT: three-material decomposition *Med. Phys.* 36 1602–9

Long Y and Fessler J A 2014 Multi-material decomposition using statistical image reconstruction for spectral CT *IEEE Trans. Med. Imaging* 33 1614–26

Maass C, Baer M and Kachelriess M 2009 Image-based dual energy CT using optimized precorrection functions: a practical new approach of material decomposition in image domain *Med. Phys.* 36 3818–29

McCollough C H, Leng S, Yu L and Fletcher J G 2015 Dual- and multi-energy CT: principles, technical approaches, and clinical applications *Radiology* **276** 637–53

Mendonca P R S, Lamb P and Sahani D V 2014 A flexible method for multi-material decomposition of dual-energy CT images *IEEE Trans. Med. Imaging* 33 99–116

 $Niu\ T, Dong\ X, Petrongolo\ M\ and\ Zhu\ L\ 2014\ Iterative\ image-domain\ decomposition\ for\ dual-energy\ CT\ \textit{Med. Phys.}\ 41\ 041901$

Persson M, Huber B, Karlsson S, Liu X, Chen H, Xu C, Yveborg M, Bornefalk H and Danielsson M 2014 Energy-resolved CT imaging with a photon-counting silicon-strip detector *Phys. Med. Biol.* **59** 6709–27

Raja A, Moghiseh M, Bateman C, de Ruiter N, Schon B, Schleich N, Woodfield T, Butler A and Anderson N 2018 Measuring identification and quantification errors in spectral CT material decomposition *Appl. Sci.* 8 1–19

Ronaldson J P, Zainon R, Scott N J A, Gieseg S P, Bulter A P, Butler P H and Anderson N G 2012 Toward quantifying the composition of soft tissues by spectral CT with medipix3 *Med. Phys.* 39 6847–57

Schmidt T G 2009 Optimal 'image-based' weighting for energy-resolved CT Med. Phys. 36 3018-27

Schmidt TG 2010 CT energy weighting in the presence of scatter and limited energy resolution Med. Phys. 37 1056-67

Schmidt T G and Petkas F 2011 Region-of-interest material decomposition from truncated energy-resolved CT Med. Phys. 38 5657–66

Siewerdsen J H and Jaffray D A 2000 Optimization of x-ray imaging geometry (with specific application to flat-panel cone-beam computed tomography) *Med. Phys.* 27 1903–14

 $Taguchi\,K\,and\,Iwanczyk\,J\,S\,2013\,Vision\,20/20: single\,photon\,counting\,x-ray\,detectors\,in\,medical\,imaging\,\textit{Med. Phys.}\, \textbf{40}\,100901$

Vedula A, Glick S and Gong X 2003 Computer simulation of CT mammography using a flat-panel imager Proc. SPIE 5030 349-60

Vieira M, Bakic P and Maidment A 2013 Effect of denoising on the quality of reconstructed images in digital breast tomosynthesis *Proc. SPIE* 8668 86680C

White D, Booz J, Griffith R, Spokas J and Wilson I 1989 Tissue substitutes in radiation dosimetry and measurement *Technical Report* ICRU-44, International Commission on Radiation Units and Measurements, Bethesda, MD

Xue Y, Ruan R, Hu X, Kuang Y, Wang J, Long Y and Niu T 2017 Statistical image-domain multimaterial decomposition for dual-energy CT Med. Phys. 44 886–901

 $Yu\ L, Liu\ X\ and\ McCollough\ C\ 2009\ Pre-reconstruction\ three-material\ decomposition\ in\ dual-energy\ CT\ Proc.\ SPIE\ 7258\ 72583V$

Zbijewski W, Gang G J, Xu J, Wang A S, Stayman J W, Taguchi K, Carrino J A and Siewerdsen J H 2014 Dual-energy cone-beam CT with a flatpanel detector: effect of reconstruction algorithm on material classification *Med. Phys.* 41 021908